COMMUNICATION

Check for updates

Engineering ferroelectric instability to achieve ultralow thermal conductivity and high thermoelectric performance in Sn₁₋ₓGeₓTe†‡

Ananya Banik,[a] Tanmoy Ghosh, [ID][a] Raagya Arora,[b] Moinak Dutta,[a] Juhi Pandey,[c] Somnath Acharya,[c] Ajay Soni, [ID][c] Umesh V. Waghmare[bd] and Kanishka Biswas [ID] *[ad]

High thermoelectric performance of a crystalline solid requires it to have low thermal conductivity which is one of the utmost material challenges. Herein, we demonstrate how the local structural distortions and the associated ferroelectric lattice instability induced soft polar phonons effectively scatter the heat carrying acoustic phonons and help achieve ultralow lattice thermal conductivity in SnTe by engineering the instability near room temperature via Ge (x = 0–30 mol%) alloying. While Sn₁₋ₓGeₓTe possesses a global cubic structure above room temperature (x < 0.5), by analysing synchrotron X-ray pair distribution functions (PDFs) we showed that local rhombohedral distortion exists which is sustained up to the studied maximum temperature (~600 K) above the ferroelectric transition (T_C = 290 K). We showed that the local rhombohedral distortions in global cubic Sn₁₋ₓGeₓTe are predominantly associated with local Ge off-centering which forms a short-range chain-like structure and scatters acoustic phonons, resulting in an ultralow lattice thermal conductivity of ~0.67 W m⁻¹ K⁻¹. In addition, Sb doping in Sn₁₋ₓGeₓTe enhances the Seebeck coefficient due to p-type carrier optimization and valence band convergence, which leads to a synergistic boost in the thermoelectric figure of merit, zT, to ~1.6 at 721 K. The concept of engineering ferroelectric instability to achieve ultralow thermal conductivity is applicable to other crystalline solids, which opens up a general opportunity to enhance the thermoelectric performance.

Innovative design of solid state structures and compositions with low thermal conductivity is the way forward to high performance thermoelectric (TE) materials, which offer an environmentally friendly solution for the recovery of waste heat in the form of electricity.[1] The crux of improving a material's thermoelectric performance involves essentially the optimization

Broader context

Heat is almost always encountered as a major waste by-product in the use of any form of energy. Thermoelectricity offers a mechanism of recovery of electricity from waste heat and is therefore a pivotal part of addressing the global energy management. Maximization of thermoelectric performance requires the optimization of three interdependent material parameters: electrical conductivity (σ), the Seebeck coefficient (S) and total thermal conductivity (κ_{total}). One of the most efficient routes is the minimization of the lattice or phonon part of κ_{total} through increased acoustic phonon scattering. We devised an efficient strategy of engineering the local structural distortions and the associated ferroelectric instability in crystalline solids which induces soft polar phonons. The strong coupling of these soft polar phonons with acoustic phonons carrying heat minimizes lattice thermal conductivity. By employing this innovative strategy in Pb-free tin telluride SnTe, we obtained ultralow lattice thermal conductivity of ~0.67 W m⁻¹ K⁻¹ in 30 mol% Ge alloyed SnTe and significantly high zT of 1.6 at 721 K after carrier optimization through Sb doping. This strategy opens up a new avenue of achieving high thermoelectric performance as many materials encompass such a ferroelectric instability.

of three interdependent material properties: electrical conductivity (σ), the Seebeck coefficient (S) and thermal conductivity (κ_{total} = electronic (κ_{el}) + lattice (κ_{lat}) thermal conductivity) which govern the dimensionless thermoelectric figure of merit, $zT = \sigma S^2 T/(\kappa_{lat} + \kappa_{el})$.[2] The reduction in κ_{lat} by devising an efficient mechanism of scattering heat carrying acoustic phonons is one of the most effective and widely used avenues for high performance thermoelectrics.[3] Innovative material design like broadband phonon scatterings based on extrinsic all-scale hierarchical nano/meso-architectures[3b,4] or intrinsic material properties,[5] *e.g.*, complex crystal structures,[6] part-crystalline part-liquid state,[7]

[a] *New Chemistry Unit, Jawaharlal Nehru Centre for Advanced Scientific Research (JNCASR), Jakkur P.O., Bangalore 560064, India. E-mail: kanishka@jncasr.ac.in*

[b] *Theoretical Sciences Unit, Jawaharlal Nehru Centre for Advanced Scientific Research (JNCASR), Jakkur P.O., Bangalore 560064, India*

[c] *School of Basic Sciences, Indian Institute of Technology Mandi, Mandi, Himachal Pradesh, 175005, India*

[d] *School of Advanced Materials, Jawaharlal Nehru Centre for Advanced Scientific Research (JNCASR), Jakkur P.O., Bangalore 560064, India*

This journal is © The Royal Society of Chemistry 2019

Energy Environ. Sci., 2019, **12**, 589–595 | 589

bonding asymmetry,[8] superionic substructures with liquid-like cation disordering,[9] lone-pair induced bond anharmonicity[10] and anisotropic layered crystal structures[11] have been employed in the past to achieve low κ_{lat}. However, in many of these approaches like the introduction of nano/meso-architectures, the reduction in κ_{lat} comes with a cost of reduced charge carrier mobility (μ) and electrical conductivity.

Here, we present a new strategy to significantly reduce the κ_{lat} by engineering the ferroelectric instability induced *via* local structural distortion in a crystalline solid. The appearance of ferroelectric lattice instability is typically marked by temperature dependent softening of polar transverse optical (TO) phonons at the center of the Brillouin zone with its energy becoming comparable to that of heat transporting acoustic phonons.[12] This results in strong acoustic-optical phonon coupling,[13] and consequently causes significant scattering of acoustic phonons,[14] and low κ_{lat} in solids. Therefore, successful deployment of the ferroelectric instability in thermoelectric solids will be an effective approach to achieve high thermoelectric performance.

We demonstrate that engineering of ferroelectric instability associated with local rhombohedral structural distortions can be used to achieve high thermoelectric performance in inorganic solids like tin telluride (SnTe). SnTe has recently emerged as an environmentally friendly alternative to PbTe for mid-temperature thermoelectric power generation.[15] The global centrosymmetric room temperature rocksalt structure of SnTe, however, has lattice instability originating from resonant bonding[16] and undergoes a temperature dependent paraelectric to ferroelectric transition with a rhombohedral ($R3m$) structure below 100 K.[17] Ferroelectricity in its rhombohedral phase originates from relative displacements of the Sn and Te sublattices along the $\langle 111 \rangle$ direction.[17,18] In the close proximity of the ferroelectric transition, SnTe exhibits softening of the zone centre (the Γ-point) TO phonon modes[16b,19] and the frequencies of these TO phonons are in fact lower in the cubic phase compared to that of the rhombohedral phase.[18d] This ferroelectric instability associated with soft TO phonons in cubic SnTe can be employed to further improve its thermoelectric performance by reducing the κ_{lat}. However, the ferroelectric phase transition in SnTe occurs in a temperature regime of $\sim$100 K, making it impractical to use the associated ferroelectric instability for thermoelectric power generation at high temperatures.

Here, we have utilized the substitution of Ge (0–30 mol%) in SnTe to strengthen its ferroelectric instability near room temperature and achieve soft phonon modes in a wide range of momenta around ferroelectric instability. $Sn_{1-x}Ge_xTe$ exhibits unstable phonon branches not only at the Brillouin zone center (a characteristic of displacive phase transition), but also at wavevectors in a large domain in the Brillouin zone. In real space, this results in chain like local off-centering of Ge in the cubic SnTe lattice. The analysis of the temperature dependent synchrotron X-ray pair distribution function (PDF) reveals that although the global structure of $Sn_{1-x}Ge_xTe$ is cubic, local rhombohedral distortion, primarily created by Ge off-centering, persists even at the highest studied temperature. We have experimentally established the presence of low frequency phonon modes (soft modes) associated with the ferroelectric instability created by this

rhombohedral distortion *via* Raman spectroscopy. Soft TO phonons associated with ferroelectric instability couple strongly with strain and scatter heat carrying acoustic phonons, and thereby reduce the κ_{lat} to $\sim$0.67 W m^{-1} K^{-1} at 300 K in $Sn_{0.7}Ge_{0.3}Te$. With synergy among ultra-low κ_{lat} and enhanced Seebeck coefficients (due to Sb doping), we achieve the highest thermoelectric figure of merit, zT, of $\sim$1.6 at 721 K in carrier optimized Sb-doped $Sn_{0.7}Ge_{0.3}Te$ ($Sn_{0.57}Sb_{0.13}Ge_{0.3}Te$). This report opens up a new avenue to inhibit thermal conduction in crystalline solids by employing ferroelectric instability associated with local structural distortions.

The room temperature powder X-ray diffraction (PXRD) patterns of $Sn_{1-x}Ge_xTe$ ($x = 0$–0.5) (Fig. 1a) confirm the face centered cubic ($Fm\bar{3}m$) structure for $x < 0.5$. The gradual increase in the intensity of odd reflections (*e.g.*, (111) peak in the marked region of Fig. S1a, ESI‡) and linear decrease in the lattice parameter from 6.32 Å in SnTe to 6.22 Å in $Sn_{0.7}Ge_{0.3}Te$ (Fig. 1b) in accordance with Vegard's law indicate the progressive substitution of Sn by Ge in the cubic SnTe structure. The increasing concentration of Ge in SnTe, however, amplifies the local distortion of the cubic structure along the $\langle 111 \rangle$ direction when the Ge concentration is below 40 mol% in SnTe. Furthermore, by increasing the Ge concentration to 50 mol%, the splitting of (111) and (220) peaks associated with the stabilization of the rhombohedral phase at room temperature is evidenced in $Sn_{0.5}Ge_{0.5}Te$ (Fig. 1a and Fig. S1a, ESI‡). The local rhombohedral distortion in the cubic structure in $Sn_{1-x}Ge_xTe$ arises from the smaller atomic radii of Ge (Ge^{2+}: 0.87 Å) compared to that of Sn
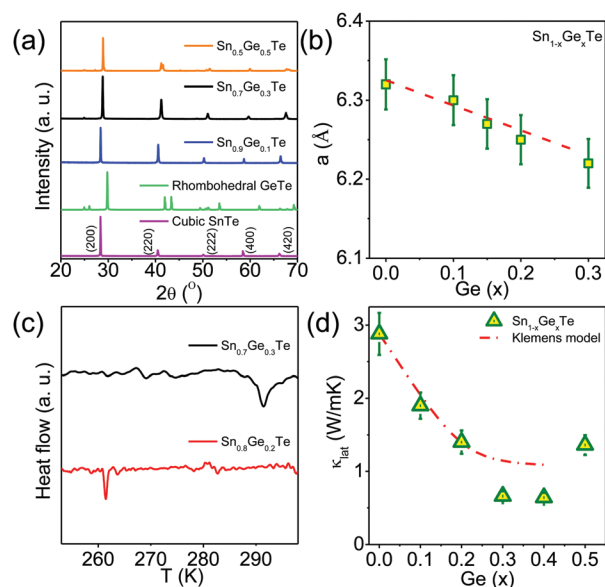

Fig. 1 (a) Powder XRD patterns of $Sn_{1-x}Ge_xTe$ ($x = 0$–0.3) samples showing Ge-concentration dependent structural phase transition represented by splitting of the (220) peak. (b) Lattice parameter (a) *vs.* Ge concentration (x) in $Sn_{1-x}Ge_xTe$ ($x = 0$–0.3). Dashed lines indicate Vegard's law for solid solutions. (c) DSC signal of $Sn_{1-x}Ge_xTe$ samples as a function of temperature. (d) Room-temperature κ_{lat} as a function of Ge alloying concentration. Red lines correspond to the predicted lattice thermal conductivities considering the mass and strain fluctuation due to Ge incorporation in the SnTe lattice based on the Klemens model.

590 | *Energy Environ. Sci.*, 2019, **12**, 589–595

This journal is © The Royal Society of Chemistry 2019

(Sn^{2+}: 0.93 Å)[20] and is the primary cause of the ferroelectric instability.[21] This behavior is further confirmed by the increase in cubic to rhombohedral phase transition temperature with increasing Ge concentration in SnTe which is evident from differential scanning calorimetry (DSC) and temperature variation of resistivity (Fig. 1c and Fig. S1b, S2, ESI‡).[22] While this cubic to rhombohedral phase transition occurs around 100 K in pristine SnTe, the 30 mol% of Ge alloying enhances the transition to near room temperature ($T_C \sim 291$ K in $x = 0.3$).

In Fig. 2, we present temperature dependent total thermal conductivity (κ_{total}) and lattice thermal conductivity (κ_{lat}) of $Sn_{1-x}Ge_xTe$ ($x = 0$–0.3) samples. GeTe alloying in SnTe substantially reduces the κ_{total} from ~ 8.66 W m^{-1} K^{-1} for SnTe to ~ 4.84 W m^{-1} K^{-1} for $Sn_{0.7}Ge_{0.3}Te$ at 300 K (Fig. 2a). The strong scattering of the heat carrying acoustic phonons by soft TO phonons associated with the ferroelectric instability in the proximity of room temperature in $Sn_{0.7}Ge_{0.3}Te$ is a possible cause for huge reduction in the κ_{lat} value from ~ 2.89 W m^{-1} K^{-1} in SnTe to ~ 0.67 W m^{-1} K^{-1} in $Sn_{0.7}Ge_{0.3}Te$ at 300 K (Fig. 2b). This κ_{lat} value of ~ 0.67 W m^{-1} K^{-1} nearly reaches the minimum theoretical value of lattice thermal conductivity, κ_{min} (~ 0.44 W m^{-1} K^{-1}) of SnTe estimated using Cahill's model.[23] While κ_{lat} values are in good agreement with the Klemens model of disordered alloys (Fig. 1d)[24] for the $Sn_{1-x}Ge_xTe$ samples for $x \leq 0.2$, indicating a predominant role of solid solution point defects in phonon scattering caused by Ge alloying in SnTe up to 20 mol% of Ge, the Klemens model largely overestimates the κ_{lat} value of $Sn_{0.7}Ge_{0.3}Te$. Backscattered electron imaging (BSE) mode field emission scanning electron microscopy (FESEM) and transmission electron microscopy (TEM) images further confirm the absence of any secondary nano/micro-precipitates (Fig. S7, ESI‡), and therefore negate the effect of nano-structuring on κ_{lat} of $Sn_{0.7}Ge_{0.3}Te$. These observations strongly imply that low frequency (soft) phonon modes associated with strong ferroelectric instability play a predominant role in the reduction of κ_{lat} in $Sn_{0.7}Ge_{0.3}Te$.

In order to understand the origin of the ultralow κ_{lat} and effects of Ge atoms in the lattice dynamics of $Sn_{1-x}Ge_xTe$, the phonon dispersion of SnTe and $Sn_{0.75}Ge_{0.25}Te$ was calculated using first-principles based Density Functional Perturbation Theory (DFPT) (Fig. 3a and b, respectively). The optical phonons of cubic SnTe (at $T = 0$ K) exhibit triply degenerate instability

with frequency (ω) of 23i cm^{-1} at the Γ-point (Fig. 3a and Fig. S9a, ESI‡). Ferroelectricity in SnTe originates from the condensation of these three unstable modes, giving a rhombohedral distortion in the cubic phase, through off-centering of Sn atoms as seen in the earlier pair distribution function (PDF)[16c] and Extended X-Ray Absorption Fine Structure (EXAFS)[16d] analysis. Phonon dispersion of cubic $Sn_{0.75}Ge_{0.25}Te$ exhibits a much stronger instability at ω of $\sim 91i$ cm^{-1} (Fig. 3b and Fig. S9b, ESI‡) at the Γ-point. An interesting feature evident in it (Fig. 3b) is the presence of unstable modes at all wave vectors in the Brillouin zone except near the R-point $\left(= \frac{\pi}{a}(1, 1, 1)\right)$. Fourier analysis of such instabilities gives a real space picture of local distortions with chain-like regions of short-range order,[25] and the size of such a distorted polar region of $\sim 1/q_c$ (q_c is the wave vector at which the branches of the unstable phonon cross zero). This signifies the local displacements of Ge atoms along the chains of Ge–Te–Sn–Te–Ge–Te in cubic $Sn_{1-x}Ge_xTe$. The character of phase transition in SnTe (unstable modes only at wave vectors close to the zone centre) thus changes from displacive to order–disorder type transition in $Sn_{0.75}Ge_{0.25}Te$.[26] Atomic displacements of the unstable phonon modes at the Γ-point of SnTe and Ge doped SnTe (the inset in Fig. 3c and Fig. S9, ESI‡) show that Ge displacements dominate the instability in $Sn_{0.75}Ge_{0.25}Te$, while the structural instability in SnTe involves displacements of both Sn and Te sublattices. The off-centred site is favored energetically due to the large ionic size difference between Sn^{2+} and Ge^{2+} (Ge^{2+}: 0.87 Å; Sn^{2+}: 0.93 Å), and higher polarization power of Ge^{2+} as compared to Sn^{2+} arising from a stronger stereochemical activity of the ns^2 lone pair in $Sn_{0.75}Ge_{0.25}Te$.[27] We calculated the Born effective charges (Z^*) which reveals higher polarization power (significant deviations

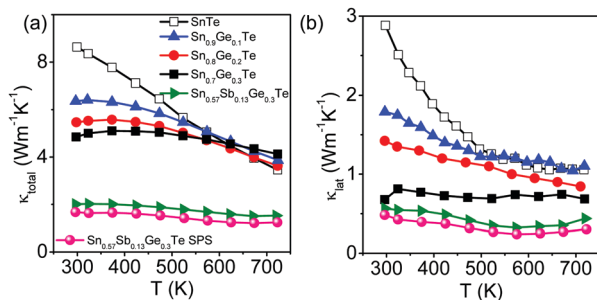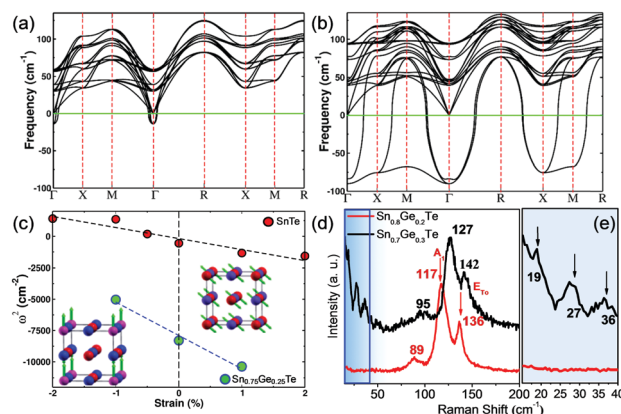Fig. 3 Phonon dispersion of (a) SnTe and (b) $Sn_{0.75}Ge_{0.25}Te$ in the centrosymmetric cubic rock salt structure at the theoretical lattice parameter without the inclusion of spin–orbit coupling (SOC), exhibiting unstable Γ-point TO mode frequencies at 23i cm^{-1} and 93i cm^{-1} respectively. (c) Dependence of the $\omega^2(\varepsilon)$ of the unstable phonon at the zone centre on the hydrostatic strain where strain is $(a - a_0)/a_0$ with $a_0 = 6.37$ Å for SnTe and $a_0 = 6.28$ Å for $Sn_{0.75}Ge_{0.25}Te$. Atomic displacements of unstable phonons at the zone centre Sn (red in colour), Te (blue in colour), and Ge (pink in colour) are shown. (d) Raman spectra of $Sn_{0.8}Ge_{0.2}Te$ and $Sn_{0.7}Ge_{0.3}Te$ at room temperature. The magnified image of the peaks enclosed in the blue dashed box is shown in (e).

Fig. 2 Temperature-dependent (a) total thermal conductivity (κ_{total}), and (b) lattice thermal conductivity (κ_{lat}) of $Sn_{1-x}Ge_xTe$ and $Sn_{0.57}Sb_{0.13}Ge_{0.3}Te$.

This journal is © The Royal Society of Chemistry 2019

Energy Environ. Sci., 2019, 12, 589–595 | 591

of Z^* from their nominal valence charges) of Ge^{2+} as compared to Sn^{2+} in $Sn_{0.75}Ge_{0.25}Te$ (Sn: $Z_{xx/yy/zz}^* = 6.63$; Ge: $Z_{xx/yy/zz}^* = 10.11$; Te: $Z_{xx/yy/zz}^* = -7.71$). Significantly stronger ferroelectric instability in $Sn_{1-x}Ge_xTe$ results in higher transition temperatures than that in SnTe.

We determined the nature and extent of cationic off-centering in SnTe and $Sn_{0.75}Ge_{0.25}Te$ by introducing small cationic displacements along the $\langle 111 \rangle$ direction, and relaxing the structure to a minimum of energy. In SnTe, relaxation of the distorted structure results in off-centering of all Sn atoms by ~ 0.06 Å and a negligible off-centering of Te atoms (~ 0.003 Å). In $Sn_{0.75}Ge_{0.25}Te$, however, Ge atoms are off-centered by ~ 0.17 Å, significantly higher than that of Sn atoms (~ 0.03–0.04 Å), accompanied by off-centering of Te atoms by ~ 0.08 Å. Thus, larger negative frequencies, along with prominent off-centering of Ge and the presence of higher polarization in $Sn_{0.75}Ge_{0.25}Te$, corroborate higher transition temperature of Ge alloyed SnTe than of SnTe.[26] Phonons at the Γ-point of the Ge off-centered structure of $Sn_{0.75}Ge_{0.25}Te$ do not exhibit any unstable modes, with the lowest three optical modes at frequencies of 29 cm^{-1}, 32 cm^{-1} and 32 cm^{-1} (related to the unstable modes of the cubic structure with $\omega = 91i$ cm^{-1}), confirming its stability at low temperature.

Thermal conductivity of a solid is controlled by anharmonic interactions between phonons. In SnTe, the interactions between the low energy optical phonons and acoustic phonons are most relevant. We estimated the strength of lattice anharmonicity quantified by strain-phonon coupling $\frac{\partial \omega^2(\varepsilon)}{\partial \varepsilon}$, where ω is the frequency of the unstable optical mode and $\varepsilon = (a - a_0)/a_0$ is the strain applied in the system, with a_0 being the theoretical lattice constant. The magnitude of $\frac{\partial \omega_0^2(\varepsilon)}{\partial \varepsilon}$ gives the third order anharmonic coupling between optical and acoustic phonons, and our estimated values are 785 cm^{-2} and 2664 cm^{-2} for SnTe and $Sn_{0.75}Ge_{0.25}Te$ (Fig. 3c), respectively. Thus, stronger anharmonic interactions between the unstable optical phonons (local polar distortions) and acoustic phonons (strain) in $Sn_{1-x}Ge_xTe$ than in SnTe result in stronger scattering of its heat carrying acoustic phonons. With increasing Ge concentration in SnTe, the sharp decrease in κ_{lat} with increasing temperature changes to a nearly temperature independent behavior of κ_{lat} of $Sn_{0.7}Ge_{0.3}Te$. This is consistent with our picture of the chain-like regions of random local off-centering of Ge atoms, which are present well above T_C, and the associated structural disorder scatters the acoustic phonons strongly.

We used Raman spectroscopy to validate the presence of soft phonon modes near room temperature in $Sn_{0.7}Ge_{0.3}Te$ (Fig. 3d). While no mode of the rocksalt structure of SnTe is Raman active,[28] local distortions of the cubic phase progressively increase with increasing Ge concentration and the off-centering of Ge in the cubic structure of SnTe is sufficient to break the symmetry and yield Raman active modes. Thus, we find optical phonon modes of $Sn_{1-x}Ge_xTe$ *via* Raman spectroscopy (Fig. 3d) at ~ 90 cm^{-1}, ~ 117 cm^{-1} and ~ 136 cm^{-1}, which are commonly observed due to Te atom vibrations.[29] Among these, the mode at 117 cm^{-1} is assigned to the A_1 symmetry, which is related to

the longitudinal optical phonon mode (LO phonon modes). The modes at 90 cm^{-1} and 136 cm^{-1} are assigned to E_{TO} (TO phonon modes). Shifts in A_1 and E_{TO} mode frequencies to higher frequencies with increasing Ge concentration are consistent with our calculated phonon dispersions (Fig. 3a and b). However, the low energy soft modes and localized modes at 19 cm^{-1}, 27 cm^{-1} and 36 cm^{-1} belong exclusively to $Sn_{0.7}Ge_{0.3}Te$, and constitute the signatures of local displacements of Ge associated with ferroelectric instability near room temperature (Fig. 3e). As shown by our DFT calculations, these modes are responsible for scattering of acoustic modes and low lattice thermal conductivity.

While the room temperature PXRD pattern of the $x = 0.3$ composition shows that the structure has a global cubic symmetry with a rocksalt structure, without any indication of rhombohedral distortion, DFT calculations strongly suggest the presence of off-centered Ge atoms which induces ferroelectric instability. To resolve this apparent contradiction, we studied the temperature dependent synchrotron X-ray Pair Distribution function (PDF) for $Sn_{0.7}Ge_{0.3}Te$ from 2.5–30 Å. The fit of total scatterings supports the global cubic symmetry of the structure (Fig. S10, ESI‡). However, when we looked into the PDF for the nearest neighbor correlation, we find that the rhombohedrally distorted structure better fits the PDF compared to the cubic model (Fig. 4a and b) which is also evident from the lower R_w value ($R_w = 0.14$) in the case of the rhombohedrally distorted structure compared to that of the cubic model ($R_w = 0.21$). This local rhombohedral distortion is predominantly created through Ge off-centering along the $\langle 111 \rangle$ direction within the global cubic model, as seen in Fig. 4d. At room temperature, Ge atoms are off-centered by ~ 0.1 Å, significantly higher than that of Sn atoms (~ 0.02 Å). The analysis of the temperature
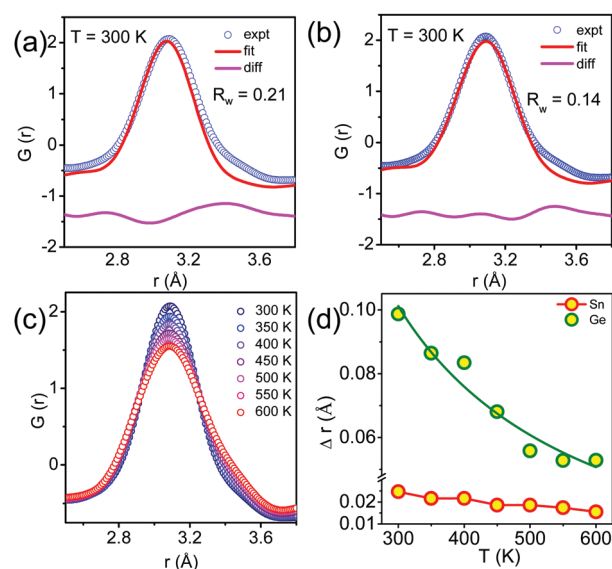

Fig. 4 Fit of the X-ray PDF for the nearest neighbor atomic correlation with the consideration of the (a) cubic structure and (b) rhombohedral distortion at room temperature in $Sn_{0.7}Ge_{0.3}Te$. Temperature evolution of the (c) X-ray PDF for the nearest neighbor atomic correlation and (d) off-centering of Sn and Ge atoms in $Sn_{0.7}Ge_{0.3}Te$ due to local distortion as obtained from X-ray PDF analysis.

592 | *Energy Environ. Sci.*, 2019, **12**, 589–595

This journal is © The Royal Society of Chemistry 2019

evolution of the nearest neighbor correlation exhibits that the amplitude of Ge off-centering decreases with increasing temperature (Fig. S11, ESI‡ and Fig. 4d). This local distortion, however, is sustained much above the ferroelectric transition temperature ($\sim 2T_C$, T_C is the ferroelectric transition temperature), as predicted from the phonon dispersion of $Sn_{0.75}Ge_{0.25}Te$. The decrease in intensity of the peaks with increasing temperature is because of increased thermal vibrations (atomic displacement parameters (ADPs)) of the atomic species (Fig. 4c and Fig. S12, ESI‡). This persistent local structural distortion and the associated ferroelectric instability strongly affect the high temperature thermal conductivity, and thus the overall thermoelectric properties. The lowering of thermal conductivity due to the presence of off-centered Ge and Hg dopants has been observed recently in the PbSe system as well.[30]

To optimize the excess p-type carrier concentration of $Sn_{1-x}Ge_xTe$, we have doped trivalent Sb^{3+} in $Sn_{0.7}Ge_{0.3}Te$, which not only optimizes the electronic transport properties but also decreases κ_{el}, and thus the κ_{total}. The PXRD patterns (Fig. S13a, ESI‡) of Sb doped $Sn_{1-x}Ge_xTe$ ($Sn_{0.7-y}Sb_yGe_{0.3}Te$, $y = 0–0.15$) confirm the solid solution nature with a linearly decreasing lattice parameter from 6.22 Å for $Sn_{0.7}Ge_{0.3}Te$ to 6.19 Å for $Sn_{0.57}Sb_{0.13}Ge_{0.3}Te$ (Fig. S13c, ESI‡). The reduction in the p-type carrier concentration (n_H) due to Sb doping is evident in Table S1, ESI.‡ Room temperature κ_{el} drastically reduces from ~ 4.16 W m^{-1} K^{-1} for $Sn_{0.7}Ge_{0.3}Te$ to ~ 1.44 W m^{-1} K^{-1} for $Sn_{0.57}Sb_{0.13}Ge_{0.3}Te$ (Fig. S15b, ESI‡). As a result, the room temperature κ_{total} reduces from 4.84 W m^{-1} K^{-1} in $Sn_{0.7}Ge_{0.3}Te$ to 2.01 W m^{-1} K^{-1} in $Sn_{0.57}Sb_{0.13}Ge_{0.3}Te$ (Fig. 2a). To further reduce thermal conductivity, we have performed mechanical grinding and spark plasma sintering (SPS) of $Sn_{0.57}Sb_{0.13}Ge_{0.3}Te$ and obtained an ultralow value of κ_{lat} of ~ 0.44 W m^{-1} K^{-1} at 728 K in $Sn_{0.57}Sb_{0.13}Ge_{0.3}Te$ (Fig. 2b).

The temperature variation of electrical conductivity (σ) of $Sn_{1-x}Ge_xTe$ exhibits a degenerate semiconducting behavior (Fig. 5a) which primarily originates from intrinsic Sn vacancies.[31] Typically, the room temperature σ value is 5989 S cm^{-1} for $Sn_{0.7}Ge_{0.3}Te$ which reduces to 2507 S cm^{-1} at 710 K. Room temperature σ decreases with increasing Ge concentration and reaches a minimum value in $Sn_{0.8}Ge_{0.2}Te$ due to the decrease in the p-type carrier concentration (n_H) (Table S1, ESI‡). The progressive substitution of Sn by Ge fills the Sn vacancies and thereby reduces the hole concentration (n_H). The $x = 0.3$ composition has a higher σ value compared to that of the $x = 0.2$ composition (Fig. 5a), despite having a higher atomic disorder, and lowest value of $d\rho/dT$ (ρ is the resistivity) at room temperature which increases on either side of this composition (Fig. S2, ESI‡). These indicate towards a possible predominant role of dielectric screening of charge carriers at room temperature in the $x = 0.3$ composition for having its ferroelectric transition in the closest proximity of room temperature. We have compared the carrier mobility of $Sn_{1-x}Ge_xTe$ with the other SnTe based materials that possess similar carrier concentrations (Table S1, ESI‡), which shows comparatively higher values of carrier mobility, μ, in Ge alloyed samples, further corroborating the increased dielectric screening of the mobile charge carriers due to impurity/defect
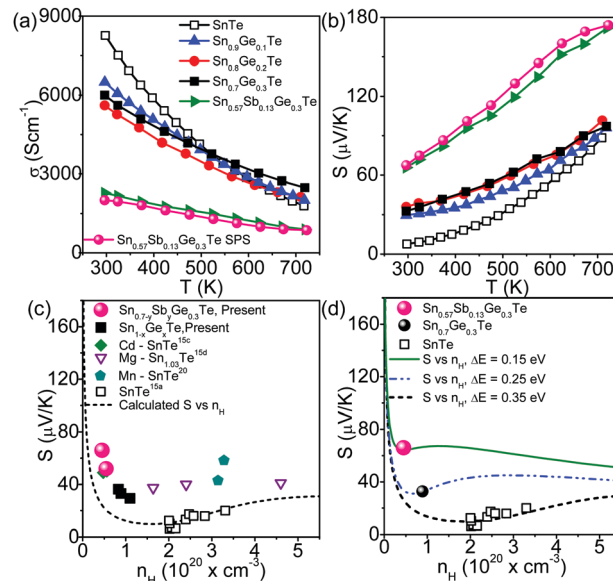

Fig. 5 (a) and (b) show the temperature dependent electrical conductivity (σ) and the Seebeck coefficient (S) of $Sn_{1-x}Ge_xTe$ and $Sn_{0.7-y}Sb_yGe_{0.3}Te$ samples. (c) Room temperature S vs. n_H plots of the present $Sn_{1-x}Ge_xTe$ and $Sn_{0.7-y}Sb_yGe_{0.3}Te$ samples. For comparison, previously reported S vs. n_H experimental data of un-doped SnTe,[15a] Cd doped SnTe,[15c] Mg alloyed SnTe,[15d] and Mn doped SnTe,[20] and the theoretical Pisarenko curve based on the VBM model are given in (c). (d) Pisarenko lines for $Sn_{0.7}Ge_{0.3}Te$ and $Sn_{0.7-y}Sb_yGe_{0.3}Te$ are calculated based on a two-valence-band model, considering reduced energy separation of valence bands via Ge alloying and Sb alloying. The experimental S vs. n_H values for $Sn_{0.7}Ge_{0.3}Te$ and $Sn_{0.7-y}Sb_yGe_{0.3}Te$ are in good agreement with the theoretical Pisarenko values confirming the modification of the electronic structure.

scattering in the proximity of paraelectric to ferroelectric phase transition.[32] A similar increase in carrier mobility due to dielectric screening has earlier been observed in complex oxides[33] and $Pb_{1-x}Sn_xSe$.[34] Further reduction in carrier concentration (Table S1, ESI‡) due to Sb doping reduces σ over the entire measured temperature range in the $Sn_{0.7-y}Sb_yGe_{0.3}Te$ ($y = 0–0.15$) samples (Fig. 5a and Fig. S16a, ESI‡). At room temperature $\sigma \sim 5989$ S cm^{-1} for $Sn_{0.7}Ge_{0.3}Te$ decreases to 2291 S cm^{-1} in $Sn_{0.57}Sb_{0.13}Ge_{0.3}Te$. The SPS processed $Sn_{0.57}Sb_{0.13}Ge_{0.3}Te$ sample exhibits a further reduction in electrical conductivity due to increased grain boundary scattering of mobile charge carriers (Fig. 5a).

The positive value of the Seebeck coefficient (S) across the measured temperature range of 300–723 K (Fig. 5b) indicates the dominant p-type charge transport in $Sn_{1-x}Ge_xTe$. Typically, the room temperature S value is ~ 32 μV K^{-1} in $Sn_{0.7}Ge_{0.3}Te$ which increases to ~ 100 μV K^{-1} at 721 K. The measured S value of SnTe is consistent with the previous reports and the theoretically calculated Pisarenko line (Fig. 5c) using a two valence band model (VBM) considering the contribution from both the non-parabolic light hole (the L point) and the parabolic heavy hole (the Σ point) valence band with energy separation (ΔE) of 0.35 eV. $Sn_{1-x}Ge_xTe$, however, shows deviation with significantly higher S values from the theoretically estimated Pisarenko line similar to the previous cases of valence band convergence.[15c,20] Experimentally measured larger principal band gaps (Fig. S17, ESI‡) additionally suggest that Ge alloying results in electronic structure modification via valence band
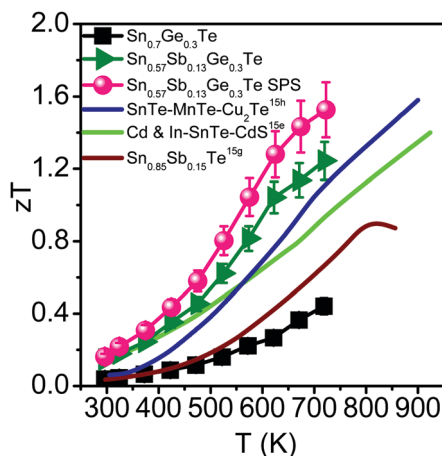
This journal is © The Royal Society of Chemistry 2019

Energy Environ. Sci., 2019, 12, 589–595 | 593

Fig. 6 Temperature-dependent zT of $Sn_{1-x}Ge_xTe$ (x = 0–0.3) and $Sn_{0.57}Sb_{0.13}Ge_{0.3}Te$ samples. For comparison, we have also plotted zT of previously reported high performance SnTe-based thermoelectric materials.

convergence. To further validate this point, we calculated the Pisarenko line considering a two valence band model by varying the energy gap (ΔE) between the light and heavy hole valence bands. The S value of $Sn_{0.7}Ge_{0.3}Te$ falls on the Pisarenko curve with ΔE = 0.25 eV (Fig. 5c and d) which indeed suggests the valence band convergence.

The reduction in the energy gap between the two valence bands (ΔE = 0.25 eV of $Sn_{0.7}Ge_{0.3}Te$ as compared to ΔE = 0.35 eV of SnTe) results in an enhanced Seebeck coefficient in $Sn_{0.7}Ge_{0.3}Te$. The Sb doping in $Sn_{0.7}Ge_{0.3}Te$ ($Sn_{0.7-y}Sb_yGe_{0.3}Te$) further enhances the Seebeck coefficient (Fig. 5b–d) because of the decrease in energy separation between the two valence bands (ΔE = 0.15 eV for $Sn_{0.57}Sb_{0.13}Ge_{0.3}Te$ in Fig. 5d). Typically, the room temperature S value of the SPS processed $Sn_{0.57}Sb_{0.13}Ge_{0.3}Te$ is ~ 68 $\mu V\ K^{-1}$ which reaches the maximum of ~ 174 $\mu V\ K^{-1}$ at 721 K. The SPS processed $Sn_{0.57}Sb_{0.13}Ge_{0.3}Te$ sample exhibits the highest power factor of σS^2 with a room temperature value of ~ 9.7 $\mu W\ cm^{-1}\ K^{-2}$ which increases to ~ 27 $\mu W\ cm^{-1}\ K^{-2}$ at 721 K (Fig. S16c, ESI‡).

Benefitting from the drastic reduction in κ_{lat} due to soft TO phonon modes generated by ferroelectric instability associated with local rhombohedral distortion created by the Ge atoms along with an enhanced Seebeck coefficient due to valence band convergence, a maximum zT of ~ 1.6 has been achieved in the SPS processed $Sn_{0.57}Sb_{0.13}Ge_{0.3}Te$ at 721 K (Fig. 6). A much higher zT is achieved in $Sn_{0.7-y}Sb_yGe_{0.3}Te$, notably in comparison with $Sn_{1-y}Sb_yTe$ and SnTe, which conclusively demonstrates the role of Ge substitution in engineering the ferroelectric-instability. Considering the hot and cold end temperature to be 720 K and 300 K, respectively, an average zT of ~ 0.9 is found in $Sn_{0.57}Sb_{0.13}Ge_{0.3}Te$ which is higher than any of the previously reported SnTe based materials in this temperature window.[15e]

Conclusions

In conclusion, we have demonstrated how the engineering of ferroelectric instability induced by local structural distortions

and softening of the TO phonon modes yield ultralow thermal conductivity in Ge alloyed SnTe. Furthermore, Sb substitution enhances the Seebeck coefficient significantly by optimizing the p-type carrier concentration and reducing the energy offset between two valence bands of SnTe. As a result of synergy between these mechanisms, zT of 1.6 is achieved in $Sn_{0.57}Sb_{0.13}Ge_{0.3}Te$ at 721 K. The strategy of improving thermoelectric performance by tuning local structural distortion and associated ferroelectric instability as demonstrated here opens up a new avenue for the development of high performance thermoelectrics. This new strategy is engaging, particularly, because it can readily be applied to further boost the thermoelectric performance of materials like SnSe and GeTe, which are close to ferroelectric instabilities.

Conflicts of interest

There are no conflicts to declare.

Acknowledgements

Notes and references

1 (a) G. Tan, L.-D. Zhao and M. G. Kanatzidis, *Chem. Rev.*, 2016, **116**, 12123–12149; (b) Z.-H. Ge, L.-D. Zhao, D. Wu, X. Liu, B.-P. Zhang, J.-F. Li and J. He, *Mater. Today*, 2016, **19**, 227–239.

2 L.-D. Zhao, V. P. Dravid and M. G. Kanatzidis, *Energy Environ. Sci.*, 2014, **7**, 251–268.

3 (a) Y. Xiao, H. Wu, W. Li, M. Yin, Y. Pei, Y. Zhang, L. Fu, Y. Chen, S. J. Pennycook, L. Huang, J. He and L.-D. Zhao, *J. Am. Chem. Soc.*, 2017, **139**, 18732–18738; (b) K. Biswas, J. He, I. D. Blum, C.-I. Wu, T. P. Hogan, D. N. Seidman, V. P. Dravid and M. G. Kanatzidis, *Nature*, 2012, **489**, 414–418; (c) M. Samanta and K. Biswas, *J. Am. Chem. Soc.*, 2017, **139**, 9382–9391.

4 G. Tan, F. Shi, S. Hao, L.-D. Zhao, H. Chi, X. Zhang, C. Uher, C. Wolverton, V. P. Dravid and M. G. Kanatzidis, *Nat. Commun.*, 2016, **7**, 12167.

5 M. K. Jana and K. Biswas, *ACS Energy Lett.*, 2018, **3**, 1315–1324.

6 G. J. Snyder and E. S. Toberer, *Nat. Mater.*, 2008, **7**, 105–114.

7 B. Li, H. Wang, Y. Kawakita, Q. Zhang, M. Feygenson, H. L. Yu, D. Wu, K. Ohara, T. Kikuchi, K. Shibata, T. Yamada, X. K. Ning, Y. Chen, J. Q. He, D. Vaknin, R. Q. Wu, K. Nakajima and M. G. Kanatzidis, *Nat. Mater.*, 2018, **17**, 226–230.

594 | *Energy Environ. Sci.*, 2019, **12**, 589–595

This journal is © The Royal Society of Chemistry 2019

8 (a) M. K. Jana, K. Pal, A. Warankar, P. Mandal, U. V. Waghmare and K. Biswas, *J. Am. Chem. Soc.*, 2017, **139**, 4350–4353; (b) M. K. Jana, K. Pal, U. V. Waghmare and K. Biswas, *Angew. Chem., Int. Ed.*, 2016, **55**, 7792–7796.

9 (a) H. Liu, X. Shi, F. Xu, L. Zhang, W. Zhang, L. Chen, Q. Li, C. Uher, T. Day and G. J. Snyder, *Nat. Mater.*, 2012, **11**, 422–425; (b) S. Roychowdhury, M. K. Jana, J. Pan, S. N. Guin, D. Sanyal, U. V. Waghmare and K. Biswas, *Angew. Chem., Int. Ed.*, 2018, **57**, 4043–4047; (c) A. A. Olvera, N. A. Moroz, P. Sahoo, P. Ren, T. P. Bailey, A. A. Page, C. Uher and P. F. P. Poudeu, *Energy Environ. Sci.*, 2017, **10**, 1668–1676.

10 D. Morelli, V. Jovovic and J. Heremans, *Phys. Rev. Lett.*, 2008, **101**, 035901.

11 (a) L.-D. Zhao, S.-H. Lo, Y. Zhang, H. Sun, G. Tan, C. Uher, C. Wolverton, V. P. Dravid and M. G. Kanatzidis, *Nature*, 2014, **508**, 373–377; (b) M. Samanta, K. Pal, P. Pal, U. V. Waghmare and K. Biswas, *J. Am. Chem. Soc.*, 2018, **140**, 5866–5872.

12 W. Cochran, *Adv. Phys.*, 1960, **9**, 387–423.

13 (a) R. M. Murphy, É. D. Murray, S. Fahy and I. Savić, *Phys. Rev. B*, 2017, **95**, 144302; (b) T. Seddon, J. M. Farley and G. A. Saunders, *Solid State Commun.*, 1975, **17**, 55–57.

14 (a) O. Delaire, J. Ma, K. Marty, A. F. May, M. A. McGuire, M. H. Du, D. J. Singh, A. Podlesnyak, G. Ehlers, M. D. Lumsden and B. C. Sales, *Nat. Mater.*, 2011, **10**, 614–619; (b) M. P. Jiang, M. Trigo, I. Savić, S. Fahy, É. D. Murray, C. Bray, J. Clark, T. Henighan, M. Kozina, M. Chollet, J. M. Glownia, M. C. Hoffmann, D. Zhu, O. Delaire, A. F. May, B. C. Sales, A. M. Lindenberg, P. Zalden, T. Sato, R. Merlin and D. A. Reis, *Nat. Commun.*, 2016, **7**, 12291.

15 (a) A. Banik, S. Roychowdhury and K. Biswas, *Chem. Commun.*, 2018, **54**, 6573–6590; (b) Q. Zhang, B. Liao, Y. Lan, K. Lukas, W. Liu, K. Esfarjani, C. Opeil, D. Broido, G. Chen and Z. Ren, *Proc. Natl. Acad. Sci. U. S. A.*, 2013, **110**, 13261–13266; (c) G. Tan, L.-D. Zhao, F. Shi, J. W. Doak, S.-H. Lo, H. Sun, C. Wolverton, V. P. Dravid, C. Uher and M. G. Kanatzidis, *J. Am. Chem. Soc.*, 2014, **136**, 7006–7017; (d) A. Banik, U. S. Shenoy, S. Anand, U. V. Waghmare and K. Biswas, *Chem. Mater.*, 2015, **27**, 581–587; (e) G. Tan, F. Shi, S. Hao, H. Chi, L.-D. Zhao, C. Uher, C. Wolverton, V. P. Dravid and M. G. Kanatzidis, *J. Am. Chem. Soc.*, 2015, **137**, 5100–5112; (f) A. Banik, U. S. Shenoy, S. Saha, U. V. Waghmare and K. Biswas, *J. Am. Chem. Soc.*, 2016, **138**, 13068–13075; (g) A. Banik, B. Vishal, S. Perumal, R. Datta and K. Biswas, *Energy Environ. Sci.*, 2016, **9**, 2011–2019; (h) W. Li, L. Zheng, B. Ge, S. Lin, X. Zhang, Z. Chen, Y. Chang and Y. Pei, *Adv. Mater.*, 2017, **29**, 1605887.

16 (a) U. V. Waghmare, N. A. Spaldin, H. C. Kandpal and R. Seshadri, *Phys. Rev. B: Condens. Matter Mater. Phys.*, 2003, **67**, 125111; (b) S. Katayama and H. Kawamura, *Solid State Commun.*, 1977, **21**, 521–524; (c) K. R. Knox, E. S. Bozin, C. D. Malliakas, M. G. Kanatzidis and S. J. L. Billinge, *Phys. Rev. B: Condens. Matter Mater. Phys.*, 2014, **89**, 014102; (d) K. V. Mitrofanov, A. V. Kolobov, P. Fons, M. Krbal, T. Shintani, J. Tominaga and T. Uruga, *Phys. Rev. B: Condens. Matter Mater. Phys.*, 2014, **90**, 134101; (e) L. Aggarwal, A. Banik, S. Anand, U. V. Waghmare, K. Biswas and G. Sheet, *J. Materiomics*, 2016, **2**, 196–202; (f) S. Lee, K. Esfarjani, T. Luo, J. Zhou, Z. Tian and G. Chen, *Nat. Commun.*, 2014, **5**, 3525.

17 M. Sist, E. M. J. Hedegaard, S. Christensen, N. Bindzus, K. F. F. Fischer, H. Kasai, K. Sugimoto and B. B. Iversen, *IUCrJ*, 2016, **3**, 377–388.

18 (a) G. S. Pawley, W. Cochran, R. A. Cowley and G. Dolling, *Phys. Rev. Lett.*, 1966, **17**, 753–755; (b) M. Iizumi, Y. Hamaguchi, K. F. Komatsubara and Y. Kato, *J. Phys. Soc. Jpn.*, 1975, **38**, 443–449; (c) K. Murase and S. Sugai, *Solid State Commun.*, 1979, **32**, 89–93; (d) C. D. O'Neill, D. A. Sokolov, A. Hermann, A. Bossak, C. Stock and A. D. Huxley, *Phys. Rev. B*, 2017, **95**, 144101.

19 S. Sugai, K. Murase and H. Kawamura, *Solid State Commun.*, 1977, **23**, 127–129.

20 G. Tan, F. Shi, S. Hao, H. Chi, T. P. Bailey, L.-D. Zhao, C. Uher, C. Wolverton, V. P. Dravid and M. G. Kanatzidis, *J. Am. Chem. Soc.*, 2015, **137**, 11507–11516.

21 J. N. Bierly, L. Muldawer and O. Beckman, *Acta Metall.*, 1963, **11**, 447–454.

22 I. Hatta and W. Rehwald, *J. Phys. C: Solid State Phys.*, 1977, **10**, 2075.

23 D. G. Cahill, S. K. Watson and R. O. Pohl, *Phys. Rev. B: Condens. Matter Mater. Phys.*, 1992, **46**, 6131–6140.

24 P. G. Klemens, *Phys. Rev.*, 1960, **119**, 507–509.

25 H. Krakauer, R. Yu, C.-Z. Wang, K. M. Rabe and U. V. Waghmare, *J. Phys.: Condens. Matter*, 1999, **11**, 3779.

26 A. I. Lebedev and I. A. Sluchinskaya, *Phys. Solid State*, 2007, **49**, 1132–1141.

27 (a) J. Trajic, A. Golubovic, M. Romcevic, N. Romcevic, S. Nikolic and N. N. Vladimir, *J. Serb. Chem. Soc.*, 2007, **72**, 55–62; (b) W. G. Zeier, A. Zevalkink, Z. M. Gibbs, G. Hautier, M. G. Kanatzidis and G. J. Snyder, *Angew. Chem., Int. Ed.*, 2016, **55**, 6826–6841.

28 L. Brillson and E. Burstein, *Phys. Rev. Lett.*, 1971, **27**, 808.

29 S. Acharya, J. Pandey and A. Soni, *Appl. Phys. Lett.*, 2016, **109**, 133904.

30 (a) Z.-Z. Luo, S. Hao, X. Zhang, X. Hua, S. Cai, G. Tan, T. P. Bailey, R. Ma, C. Uher, C. Wolverton, V. P. Dravid, Q. Yan and M. G. Kanatzidis, *Energy Environ. Sci.*, 2018, **11**, 3220–3230; (b) J. M. Hodges, S. Hao, J. A. Grovogui, X. Zhang, T. P. Bailey, X. Li, Z. Gan, Y.-Y. Hu, C. Uher, V. P. Dravid, C. Wolverton and M. G. Kanatzidis, *J. Am. Chem. Soc.*, 2018, **140**, 18115–18123.

31 U. Jun-ichi, J. Manu and O. Toshihiro, *Jpn. J. Appl. Phys.*, 1962, **1**, 277.

32 X. Zhang and Y. Pei, *npj Quantum Mater.*, 2017, **2**, 68.

33 W. Siemons, M. A. McGuire, V. R. Cooper, M. D. Biegalski, I. N. Ivanov, G. E. Jellison, L. A. Boatner, B. C. Sales and H. M. Christen, *Adv. Mater.*, 2012, **24**, 3965–3969.

34 P. Dziawa, B. J. Kowalski, K. Dybko, R. Buczko, A. Szczerbakow, M. Szot, E. Łusakowska, T. Balasubramanian, B. M. Wojek, M. H. Berntsen, O. Tjernberg and T. Story, *Nat. Mater.*, 2012, **11**, 1023–1027.

This journal is © The Royal Society of Chemistry 2019

Energy Environ. Sci., 2019, **12**, 589–595 | 595